Moving mesh finite difference methods for non-monotone two-phase flows in porous media

Hong Zhang

Supervisor: Paul A. Zegeling

Department of Mathematics, Utrecht University, NL

27 May - 1 June, 2018 · Banff

Universiteit Utrecht

Outline

Background studies

Mathematical model

Traveling wave results

The adaptive moving mesh methods

Conclusions

Pouring water into sand

Water and sands, figures are downloaded from Google.

Monotonic flow

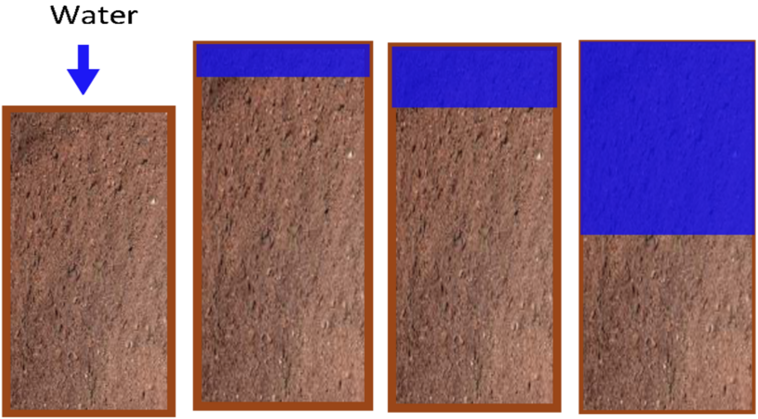

Universiteit Utrecht

The formation of gravity-driven fingers following ponded infiltration

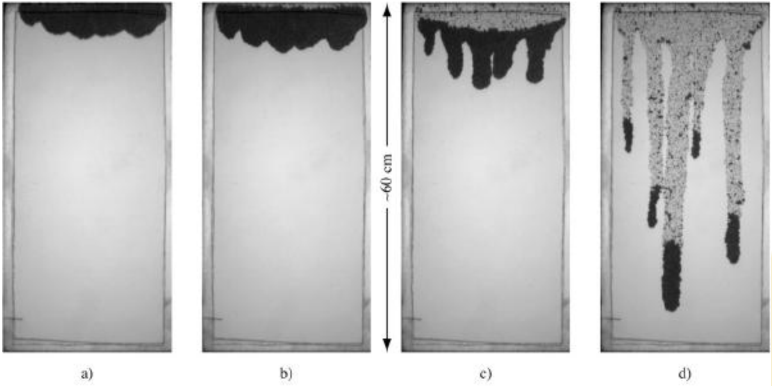

Gravity driven fingers[1].

[1] MJ Nicholl and RJ Glass. "Infiltration into an Analog Fracture". In: *Vadose Zone Journal* 4.4 (2005), pp. 1123–1151.

Finger structure

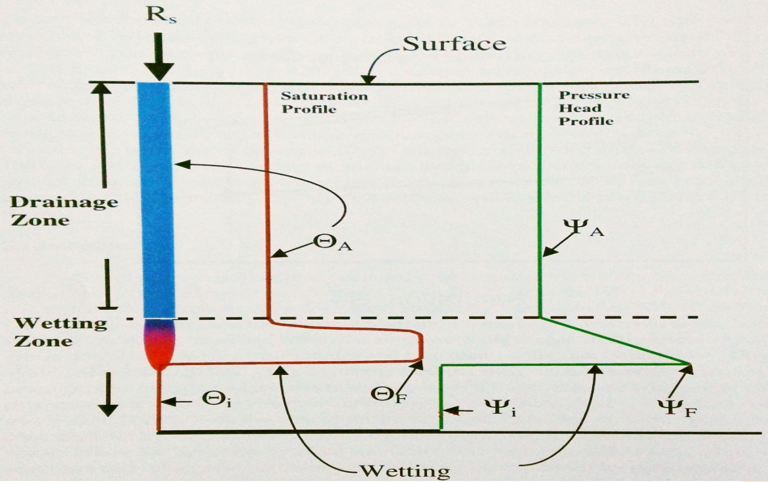

An illustration of non-monotonic finger pattern[2].

[2] Mehdi Eliassi. "On continuum -scale numerical simulation gravity -driven fingers in unsaturated porous material". PhD thesis. 2001.

Universiteit Utrecht

Mathematical Model

- Mass conservation law:

$$\frac{\partial(\phi\rho_\alpha S_\alpha)}{\partial t} + \frac{\partial}{\partial x}(\rho_\alpha v_\alpha) = 0, \quad \alpha = w, n \tag{1.1}$$

where ϕ is the porosity of the porous medium, S_α, ρ_α and v_α are the saturation, density and volumetric velocity of phase α.

- Darcy's law:

$$v_\alpha = -\frac{k_{r\alpha}K}{\mu_\alpha}\frac{\partial}{\partial x}(p_\alpha - \rho_\alpha g x) = -\lambda_\alpha(\frac{\partial p_\alpha}{\partial x} - \rho_\alpha g), \quad \alpha = w, n \tag{1.2}$$

where g is the gravitational acceleration constant, K is the intrinsic permeability, $k_{r\alpha}$, μ_α, $\lambda_\alpha = \frac{k_{r\alpha}K}{\mu_\alpha}$ and p_α are the relative permeability function, viscosity, mobility and pressure of phase α, respectively.

Mathematical Model

- Mass conservation law:

$$\frac{\partial(\phi\rho_\alpha S_\alpha)}{\partial t} + \frac{\partial}{\partial x}(\rho_\alpha v_\alpha) = 0, \quad \alpha = w, n \tag{1.1}$$

where ϕ is the porosity of the porous medium, S_α, ρ_α and v_α are the saturation, density and volumetric velocity of phase α.

- Darcy's law:

$$v_\alpha = -\frac{k_{r\alpha}K}{\mu_\alpha}\frac{\partial}{\partial x}(p_\alpha - \rho_\alpha g x) = -\lambda_\alpha\left(\frac{\partial p_\alpha}{\partial x} - \rho_\alpha g\right), \quad \alpha = w, n \tag{1.2}$$

where g is the gravitational acceleration constant, K is the intrinsic permeability, $k_{r\alpha}$, μ_α, $\lambda_\alpha = \frac{k_{r\alpha}K}{\mu_\alpha}$ and p_α are the relative permeability function, viscosity, mobility and pressure of phase α, respectively.

Define the total velocity $v_T = v_n + v_w$ and fractional flow rate of the wetting phase $f = \frac{\lambda_w}{\lambda_w + \lambda_n}$, then the velocity of the wetting phase can be expressed by

$$v_w = v_T f[1 + \frac{\lambda_n}{v_T}(\frac{\partial}{\partial x}(p_n - p_w) + (\rho_w - \rho_n)g)]. \qquad (1.3)$$

By substituting v_w into mass equation for the wetting phase, we obtain

$$\phi \frac{\partial S_w}{\partial t} + \frac{\partial}{\partial x}\left[v_T f[1 + \frac{\lambda_n}{v_T}(\frac{\partial}{\partial x}(p_n - p_w) + (\rho_w - \rho_n)g)]\right] = 0. \qquad (1.4)$$

Universiteit Utrecht

Dynamic capillary pressure relationship

- Under equilibrium conditions:

$$p_n - p_w = p_c = P_c(S_w). \tag{1.5}$$

- Under non-equilibrium conditions, Hassanizadeh (1990)[3] proposed:

$$p_n - p_w = P_c(S_w) - \tau(S_w)\frac{\partial S_w}{\partial t}. \tag{1.6}$$

The dynamic coefficient τ $[\mathrm{Pa\,s}]$ is also known as damping coefficient and may still be a function of saturation.

[3] S Majid Hassanizadeh and William G Gray. "Mechanics and thermodynamics of multiphase flow in porous media including interphase boundaries". In: *Advances in water resources* 13.4 (1990), pp. 169–186.

Dynamic capillary pressure relationship

- Under equilibrium conditions:

$$p_n - p_w = p_c = P_c(S_w). \tag{1.5}$$

- Under non-equilibrium conditions, Hassanizadeh (1990)[3] proposed:

$$p_n - p_w = P_c(S_w) - \tau(S_w)\frac{\partial S_w}{\partial t}. \tag{1.6}$$

The dynamic coefficient τ $[\mathrm{Pa\,s}]$ is also known as damping coefficient and may still be a function of saturation.

[3] S Majid Hassanizadeh and William G Gray. "Mechanics and thermodynamics of multiphase flow in porous media including interphase boundaries". In: *Advances in water resources* 13.4 (1990), pp. 169–186.

Model 1: Dynamic capillary pressure model

Adding the dynamic capillary pressure relationship to the two-phase flow equation gives:

$$\phi \frac{\partial S_w}{\partial t} + \frac{\partial}{\partial x}\Big[q f(S_w) + \lambda_n(S_w) f(S_w)\Big(\frac{\partial}{\partial x}\big(P_c(S_w) - \tau \frac{\partial S_w}{\partial t}\big) + (\rho_w - \rho_n) g\Big)\Big] = 0. \tag{1.7}$$

Universiteit Utrecht

Finger structure

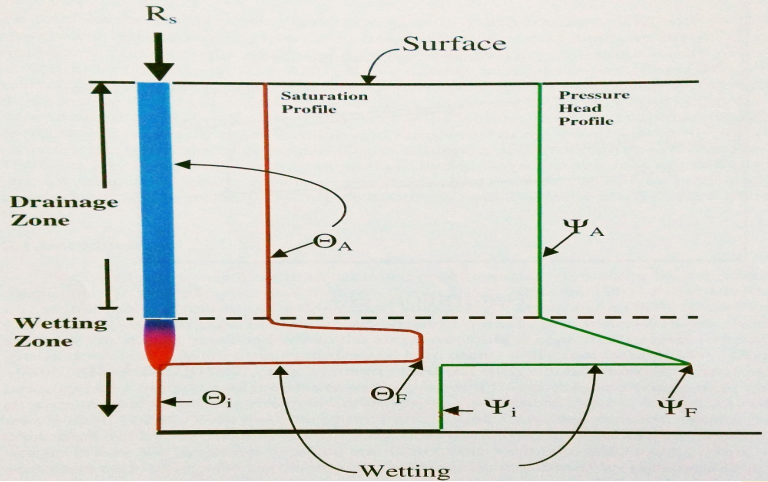

An illustration of non-monotonic finger pattern[4].

[4] Mehdi Eliassi. "On continuum -scale numerical simulation gravity -driven fingers in unsaturated porous material". PhD thesis. 2001.

Hysteresis in capillary pressure

Many studies have shown that the relationship between capillary pressure and saturation also depends on the history of flow displacement and on the rate of change of saturation.

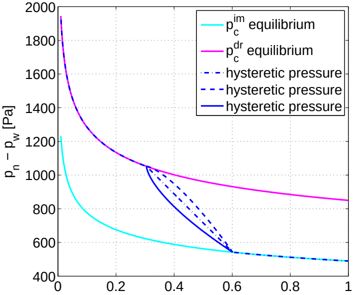

Figure 1: Capillary pressure and hysteresis loops.

Model 2: A simplified hysteresis model

The hysteresis operator

$$P_c^{hyst} : S_w(\cdot) \to p_c(\cdot). \tag{1.8}$$

In the drainage process, when S_w decreases, p_c follows the drainage pressure-saturation curve $P_c^{dr}(S_w)$. In the imbibition process, when S_w increases, p_c follows the imbibition pressure-saturation curve $P_c^{im}(S_w)$. In this hysteresis model, between the drainage and imbibition curves, p_c and S_w evolve as

$$\frac{\partial p_c}{\partial t} = -\beta \frac{\partial S_w}{\partial t}, \tag{1.9}$$

The discretization of Eq. (1.9) is

$$p_c^n = p_c^{n-1} - \beta(S_w^n - S_w^{n-1}). \tag{1.10}$$

Model 2: A simplified hysteresis model

The algorithm for computing p_c is as follows

1. Set $p_c^n = p_c^{n-1} - \beta(S_w^n - S_w^{n-1})$.
2. If $p_c^n < P_c^{im}(S_w^n)$, set $p_c^n = P_c^{im}(S_w^n)$.
3. If $p_c^n > P_c^{dr}(S_w^n)$, set $p_c^n = P_c^{dr}(S_w^n)$. The above algorithm is denoted as $p_c^n = P_c^{hyst}(S_w^n)$.

   Combining capillary pressure hysteresis with the dynamic capillary pressure relationship we obtain

$$p_n - p_w = P_c^{hyst}(S_w) - \tau \frac{\partial S_w}{\partial t}. \qquad (1.11)$$

   Substituting the hysteretic relationship into the two phase flow equation we get Model 2.

Model 2: A simplified hysteresis model

The algorithm for computing p_c is as follows

1. Set $p_c^n = p_c^{n-1} - \beta(S_w^n - S_w^{n-1})$.
2. If $p_c^n < P_c^{im}(S_w^n)$, set $p_c^n = P_c^{im}(S_w^n)$.
3. If $p_c^n > P_c^{dr}(S_w^n)$, set $p_c^n = P_c^{dr}(S_w^n)$. The above algorithm is denoted as $p_c^n = P_c^{hyst}(S_w^n)$.

   Combining capillary pressure hysteresis with the dynamic capillary pressure relationship we obtain

$$p_n - p_w = P_c^{hyst}(S_w) - \tau \frac{\partial S_w}{\partial t}. \qquad (1.11)$$

   Substituting the hysteretic relationship into the two phase flow equation we get Model 2.

Universiteit Utrecht

Model 2: A simplified hysteresis model

The algorithm for computing p_c is as follows

1. Set $p_c^n = p_c^{n-1} - \beta(S_w^n - S_w^{n-1})$.
2. If $p_c^n < P_c^{im}(S_w^n)$, set $p_c^n = P_c^{im}(S_w^n)$.
3. If $p_c^n > P_c^{dr}(S_w^n)$, set $p_c^n = P_c^{dr}(S_w^n)$. The above algorithm is denoted as $p_c^n = P_c^{hyst}(S_w^n)$.

   Combining capillary pressure hysteresis with the dynamic capillary pressure relationship we obtain

$$p_n - p_w = P_c^{hyst}(S_w) - \tau \frac{\partial S_w}{\partial t}. \tag{1.11}$$

Substituting the hysteretic relationship into the two phase flow equation we get Model 2.

Hysteresis in dynamic coefficient τ

Experimental studies in Mirzaei et al. 2013[5] suggest that τ is also hysteretic.

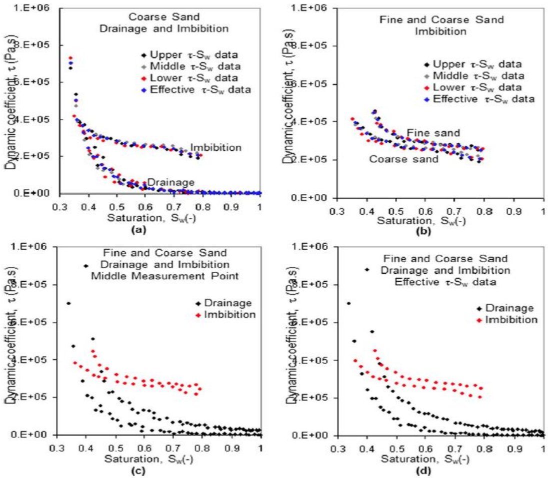

Figure 2: Hysteresis in drainage and imbibition τ-S_w curves (Mirzaei et al. 2013)

Universiteit Utrecht

Hysteresis in dynamic coefficient τ

Assume in the hysteresis process τ decreases from τ^{im} to τ^{dr}. Since τ^{hyst} may possibly due to the hysteresis in the retention pressure curve Sakaki et al. 2010[6], for simplicity, we introduce τ^{hyst} as

$$\tau^{hyst} = (\tau^{im} - \tau^{dr})[\frac{P_c^{hyst}(S_w) - \frac{1}{2}(P_c^{im}(S_w) + P_c^{dr}(S_w))}{P_c^{im}(S_w) - P_c^{dr}(S_w)} + \frac{1}{2}] + \tau^{dr}. \quad (1.12)$$

Substituting the dynamic capillary pressure with hysteresis and hysteretic dynamic coefficient into the two phase flow equation will result in Model 3 with hystereresis in both τ and p_c.

[6] Toshihiro Sakaki, Denis M O'Carroll, and Tissa H Illangasekare. "Direct quantification of dynamic effects in capillary pressure for drainage–wetting cycles". In: *Vadose Zone Journal* 9.2 (2010), pp. 424–437.

Reformulation of the non-equilibrium equation

Denote $p = p_n - p_w$, the non-equilibrium equation can be rewritten as

$$\begin{cases} \phi \dfrac{P_c(S_w) - p}{\tau} + \dfrac{\partial}{\partial x}[qf(S_w) + \lambda_n(S_w) f(S_w)(\dfrac{\partial p}{\partial x} + (\rho_w - \rho_n)g)] = 0, \\ \dfrac{\partial S_w}{\partial t} = \dfrac{P_c(S_w) - p}{\tau}. \end{cases} \tag{1.13}$$

Since Model 2 and Model 3 are incorporated with the capillary pressure hysteresis, we replace $P_c(S_w)$ in Eq. (1.13) by $P_c^{hyst}(S_w)$ when solving these two models and replace τ by τ^{hyst} when solving Model 3.

Universiteit Utrecht

Numerical results of three models

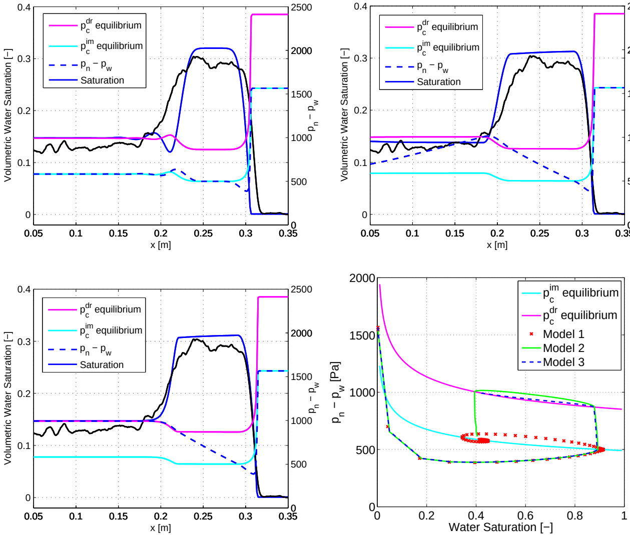

Top left: Model 1, top right: Model 2, bottom left: Model 3, bottom right: comparisons between three models. Black curves: experimental results from [DiCarlo 2004]

Universiteit Utrecht

Comparisions between Model 1, 2, 3 and experiments for different flux rates[7]

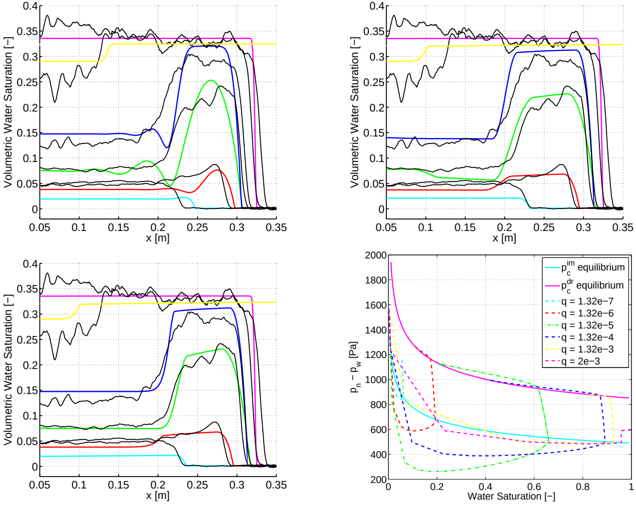

[7] David A DiCarlo. "Experimental measurements of saturation overshoot on infiltration". In: *Water Resources Research* 40.4 (2004), W04215.

1D Modified Buckley-Leverett equation

Let u be the wetting phase saturation S_w, the two-phase flow equation with dynamic capillary pressure can be rewritten as

$$\frac{\partial u}{\partial t} + \frac{\partial F(u)}{\partial x} = -\frac{\partial}{\partial x}[H(u)\frac{\partial}{\partial x}(p_c(u) - \tau\frac{\partial u}{\partial t})]. \qquad (2.1)$$

$$F(u) = \frac{1}{\phi}f(u)[v_T + \lambda_n(u)(\rho_w - \rho_n)g], \qquad (2.2)$$

$$H(u) = \frac{1}{\phi}\lambda_n(u)f(u). \qquad (2.3)$$

Equation (2.1) is also called the Modified Buckley-Leverett equation (MBLE).

Riemann problem

$$u(x,0) = \begin{cases} u_l, & x \leq 0, \\ u_r, & x > 0, \end{cases} \tag{3.1}$$

With different combinations of (u_l, u_r, τ), the MBL equation may have different types of solutions.

Traveling wave results

Let $\eta = x - st$ and substituting $u(\eta)$ into the MBLE results in a third order ODE

$$\begin{cases} -su' + [F(u)]' = -[H(u)p_c'(u)u']' - s\tau[H(u)u'']', \\ u(-\infty) = u_l, \quad u(\infty) = u_r, \quad u_l, u_r \in [0,1], \end{cases} \tag{3.2}$$

Assuming $u'(\pm\infty) = 0, u''(\pm\infty) = 0$, integrating this equation over (η, ∞) gives

$$\begin{aligned} &-s(u-u_r) + [F(u) - F(u_r)] = -H(u)p_c'(u)u' - s\tau H(u)u'', \\ &u(-\infty) = u_l, \quad u(\infty) = u_r, \end{aligned} \tag{3.3}$$

with s determined by the Rankine-Hugoniot condition $s = \frac{F(u_l)-F(u_r)}{u_l-u_r}$.

Universiteit Utrecht

Traveling wave results

When $F(u) = \frac{u^2}{u^2+M(1-u)^2}, H(u) = \epsilon^2, p_c(u) = -\frac{u}{\epsilon}$, Van Duijn et al. 2007[8], proved that the existence of the TW solution depends on the values of (u_l, u_r, τ).

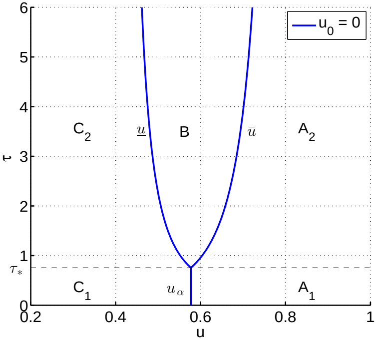

Figure 3: Bifurcation diagram.

[8] CJ van Duijn, LA Peletier, and IS Pop. "A new class of entropy solutions of the Buckley-Leverett equation". In: *SIAM Journal on Mathematical Analysis* 39.2 (2007), pp. 507–536.

Traveling wave results

Table 1: Results summarized from van Duijn et al. 2007.

Region	Solution description
$(u_B, \tau) \in A_1$	Rarefaction wave from u_B down to u_α trailing an admissible Lax shock from u_α down to u_0
$(u_B, \tau) \in A_2$	Rarefaction wave from u_B down to $\bar{u}$ trailing an undercompressive shock from $\bar{u}$ down to u_0
$(u_B, \tau) \in B$	An admissible Lax shock from u_B up to $\bar{u}$ (may exhibit oscillations near $u_l = u_B$) trailing an undercompressive shock from $\bar{u}$ down to u_0
$(u_B, \tau) \in C_1$	An admissible Lax shock from u_B down to u_0
$(u_B, \tau) \in C_2$	An admissible Lax shock from u_B down to u_0 (may exhibit oscillations near $u_l = u_B$

Example

Consider flux function $F(u) = \frac{u^2}{u^2+M(1-u)^2}[v_T + C(1-u^2)]$, where $M = 10$, $C = 10$.
The initial condition is taken as

$$u(x,0) = u_0 + 0.5(u_B - u_0)(1.0 - \tanh(200x)), \quad x \in [-0.1, 1.1]. \tag{3.4}$$

Example

Influence of flux rate:
$\tau = 3.3812, v_T = 1.0, 0.6, 0.4, 0.1, u_0 = 0, T = 1.$

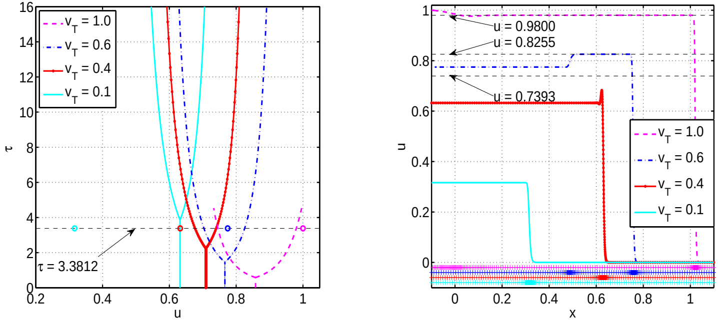

Figure 4: Bifurcation diagrams (left) and numerical solutions (right).

The adaptive moving mesh method

For a scalar solution u,

1. the popular arc-length type monitor reads

$$\omega = \sqrt{1 + \alpha |u_x|^2}. \tag{4.1}$$

2. Consider an adaptive smooth monitor function

$$\omega = (1-\beta)\alpha(t) + \beta |u_\xi|^{\frac{1}{m}}, \tag{4.2}$$

with $\alpha(t) = \frac{1}{|\Omega_c|} \int_{\Omega_c} |u_\xi|^{\frac{1}{m}} \mathrm{d}\xi$, β is the ratio of points in the critical areas.
To equidistribute the monitor function, we adopt a moving mesh PDE (MMPDE) with smoothing,

$$\frac{\partial}{\partial \xi}\left(\frac{\dot{\tilde{n}}}{\omega}\right) = -\frac{1}{\tau_s}\frac{\partial}{\partial \xi}\left(\frac{\tilde{n}}{\omega}\right), \quad \tilde{n} = [\mathcal{I} - \sigma_s(\sigma_s+1)(\Delta\xi)^2 \frac{\partial^2}{\partial \xi^2}]n. \tag{4.3}$$

The adaptive moving mesh method

For a scalar solution u,

1. the popular arc-length type monitor reads

$$\omega = \sqrt{1 + \alpha |u_x|^2}. \tag{4.1}$$

2. Consider an adaptive smooth monitor function

$$\omega = (1 - \beta)\alpha(t) + \beta |u_\xi|^{\frac{1}{m}}, \tag{4.2}$$

with $\alpha(t) = \frac{1}{|\Omega_c|} \int_{\Omega_c} |u_\xi|^{\frac{1}{m}} \mathrm{d}\xi$, β is the ratio of points in the critical areas.
To equidistribute the monitor function, we adopt a moving mesh PDE (MMPDE) with smoothing,

$$\frac{\partial}{\partial \xi}\left(\frac{\dot{\tilde{n}}}{\omega}\right) = -\frac{1}{\tau_s}\frac{\partial}{\partial \xi}\left(\frac{\tilde{n}}{\omega}\right), \quad \tilde{n} = [\mathcal{I} - \sigma_s(\sigma_s + 1)(\Delta\xi)^2 \frac{\partial^2}{\partial \xi^2}]n. \tag{4.3}$$

Discretizations

Applying the second order centered finite difference scheme to the MMPDE (4.3) in the space direction yields

$$\begin{cases} \dfrac{[\mathcal{I}-\sigma_s(\sigma_s+1)\delta_{xx}](\dot{x}_{i+1}-\dot{x}_i)}{\omega_{i+1/2}(x_{i+1}-x_i)^2}-\dfrac{[\mathcal{I}-\sigma_s(\sigma_s+1)\delta_{xx}](\dot{x}_i-\dot{x}_{i-1})}{\omega_{i-1/2}(x_i-x_{i-1})^2}= \\ \dfrac{1}{\tau_s}\left[\dfrac{[\mathcal{I}-\sigma_s(\sigma_s+1)\delta_{xx}]\frac{1}{x_{i+1}-x_i}}{\omega_{i+1/2}}-\dfrac{[\mathcal{I}-\sigma_s(\sigma_s+1)\delta_{xx}]\frac{1}{x_i-x_{i-1}}}{\omega_{i-1/2}}\right], \quad i=2,\cdots,N-2, \\ \dot{x}_{i+1}-2\dot{x}_i+\dot{x}_{i-1}=0, \quad i=1,N-1, \\ \dot{x}_0=\dot{x}_N=0, \end{cases} \tag{4.4}$$

where δ_{xx} is the second-order difference operator and $\dot{n}_i=-\frac{\dot{x}_{i+1}-\dot{x}_i}{(x_{i+1}-x_i)^2}, i=0,1,\cdots,N-1.$
The transformed physical PDE

$$(\mathcal{I}-\tau\frac{\partial}{\partial x}H(u)\frac{\partial}{\partial x})(\dot{u}-u_x\dot{x})+\frac{\partial}{\partial x}F(u)+\frac{\partial}{\partial x}[H(u)\frac{\partial}{\partial x}p_c(u)]=0, \tag{4.5}$$

is also discretized using the second-order centered difference scheme.

Example 1

Consider $M = 0.5, \epsilon = 10^{-3}$, $\tau = 5$ and initial condition

$$u(x,0) = \begin{cases} 0.25, & x \in [0, 0.75], \\ 0.66, & x \in (0.75, 2.25), \\ 0, & x \in [2.25, 3]. \end{cases} \tag{4.6}$$

Example 1

Moving mesh solutions (top left); $-u_x$ at the right boundary of the plateau (top right); zoom in at the basin area (bottom left) and at the plateau area (bottom right).

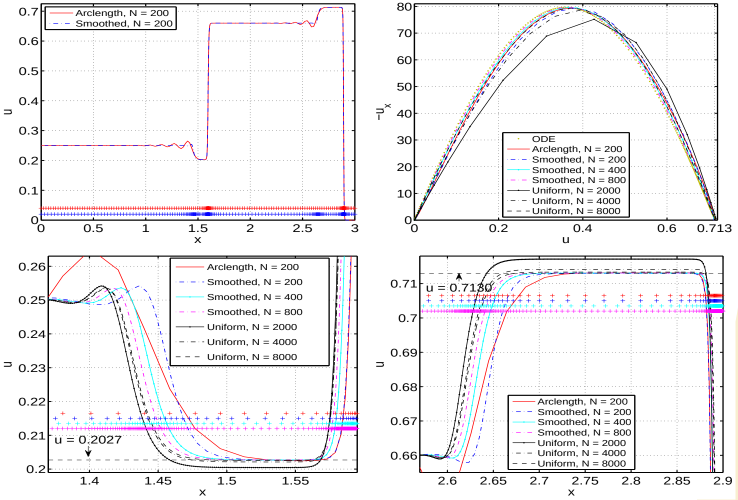

Grid trajectories

Left: adaptive smoothed monitor; right: arc-length type monitor.

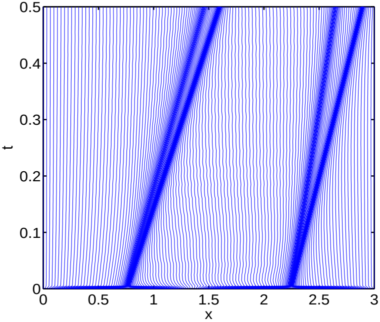

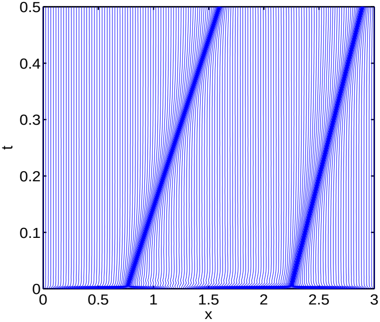

The Brooks-Corey model

Table 2: Constants and Brooks-Corey models.

Density $[\mathrm{kg\ m^{-3}}]$	$\rho_w = 998.21$	$\rho_n = 1.2754$
Viscosity $[\mathrm{kg\ m^{-1} s^{-1}}]$	$\mu_w = 1.002\text{e-}03$	$\mu_n = 1.82\text{e-}05$
Mobility $[\mathrm{m\ s\ kg^{-1}}]$	$\lambda_w = \frac{K k_{rw}}{\mu_w}$	$\lambda_n = \frac{K k_{rn}}{\mu_n}$
Constants	$g = 9.81\ [\mathrm{m\ s^{-2}}]$	$K = \frac{\kappa \mu_w}{\rho_w g}\ [\mathrm{m^2}]$
	Capillary pressure	Relative permeability
Brooks-Corey model	$S_e = \frac{S_w - S_{wr}}{1 - S_{wr}}$ $p_c = p_d S_e^{-\frac{1}{\lambda}}$, for $p_c > p_d$	$k_{rw} = S_e^{\frac{2+3\lambda}{\lambda}}$ $k_{rn} = (1 - S_e)^2 (1 - S_e^{\frac{2+\lambda}{\lambda}})$

Numerical solutions of the MBL equation using the Brooks-Corey model

Table 3: Travelling wave results for $u_0 = 0.003, 0.03$ with $v_T = 1.32 \times 10^{-4}$ $[\mathrm{ms}^{-1}]$

u_0	u_B	τ	Wave description
0.003	0.4212	1246	Non-monotone plateau
0.03	0.4212	1246	Non-monotone overshoot
0.03	0.4212	5271	Non-monotone plateau

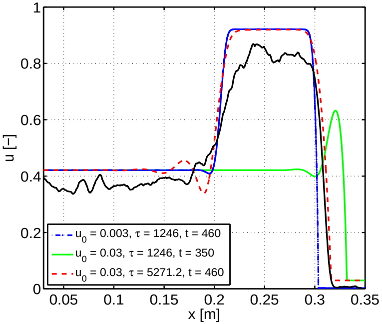

Figure 5: Comparisons between experimental result in DiCarlo 2004 and numerical solutions obtained for $(u_0, \tau, t) = (0.003, 1246, 460)$, $(0.03, 1246, 350)$, $(0.03, 5271, 460)$ using moving mesh method with $N = 800$.

Universiteit Utrecht

2D Modified Buckley-Leverett equation

The 2D MBL equation reads

$$\frac{\partial u}{\partial t} + \frac{\partial}{\partial x} F(u) + \frac{\partial}{\partial z} G(u) + \nabla \cdot [D(u) \nabla u] - \tau \nabla \cdot [H(u) \nabla \frac{\partial u}{\partial t}] = 0, \tag{4.7}$$

where

$$F(u) = \frac{1}{\phi} f_w(u) v_T^x, \qquad G(u) = \frac{1}{\phi} f_w(u) [v_T^z - \lambda_n(u)(\rho_w - \rho_n) g],$$

$$D(u) = \frac{1}{\phi} \lambda_n(u) f_w(u) P_c'(u), \qquad H(u) = \frac{1}{\phi} \lambda_n(u) f_w(u).$$

Transformation of physical equation

Based on the quasi-Lagrangian approach, we transform the MBLE from the physical coordinate (x, z) to the computational coordinate (ξ, η),

$$
\begin{aligned}
& u_t + \frac{1}{J}\big(\underbrace{z_\eta F(u) - x_\eta G(u)}_{\tilde{F}}\big)_\xi + \frac{1}{J}\big(\underbrace{x_\xi G(u) - y_\xi F(u)}_{\tilde{G}}\big)_\eta \\
& + \frac{1}{J}\Big[\big(\underbrace{\frac{D(u)}{J}(z_\eta^2 u_\xi + x_\eta^2 u_\xi - z_\xi z_\eta u_\eta - x_\xi x_\eta u_\eta)}_{R}\big)_\xi \\
& + \big(\underbrace{\frac{D(u)}{J}(z_\xi^2 u_\eta + x_\xi^2 u_\eta - z_\xi z_\eta u_\xi - x_\xi x_\eta u_\xi)_\eta}_{S}\big)\Big] \\
& - \frac{\tau}{J}\Big[\big(\underbrace{\frac{H(u)}{J}(z_\eta^2 u_{t\xi} + x_\eta^2 u_{t\xi} - z_\xi z_\eta u_{t\eta} - x_\xi x_\eta u_{t\eta})}_{P}\big)_\xi \\
& - \big(\underbrace{\frac{H(u)}{J}(z_\xi^2 u_{t\eta} + x_\xi^2 u_{t\eta} - z_\xi z_\eta u_{t\xi} - x_\xi x_\eta u_{t\xi})}_{Q}\big)_\eta\Big] = 0.
\end{aligned}
$$

Discretization of flux terms

The advection terms are discretized into conservation forms, taking $\tilde{F}(u)_\xi$ as an example:

$$\bar{\tilde{F}}_{\xi i,j} = \frac{\bar{\tilde{F}}^n_{i+1/2,j} - \bar{\tilde{F}}^n_{i-1/2,j}}{\Delta\xi}, \quad \bar{\tilde{F}}_{i+1/2,j} = \bar{\tilde{F}}(u^-_{i+1/2,j}, u^+_{i+1/2,j}).$$

For the discretization of the flux terms, we employ

1. a central difference scheme,

$$\bar{\tilde{F}}(u^{-}_{i+1/2,j}, u^{+}_{i+1/2,j}) = \bar{\tilde{F}}(u_{i,j}, u_{i+1,j}) \tag{4.8}$$

$$= \frac{1}{2}[\tilde{F}(u_{i,j}) + \tilde{F}(u_{i+1,j})], \tag{4.9}$$

2. a standard local Lax-Friedrichs (LLF) scheme,

$$\bar{\tilde{F}}(u^{-}_{i+1/2,j}, u^{+}_{i+1/2,j}) = \frac{1}{2}[\tilde{F}(u^{-}_{i+1/2,j}) + \tilde{F}(u^{+}_{i+1/2,j})$$

$$- \max|\tilde{F}_u| \cdot (u^{+}_{i+1/2,j} - u^{-}_{i+1/2,j})], \tag{4.10}$$

$$u^{-}_{i+\frac{1}{2},j} = u_{i,j}, \quad u^{+}_{i+\frac{1}{2},j} = u_{i+1,j},$$

Universiteit Utrecht

For the discretization of the flux terms, we employ

1. a central difference scheme,

$$\bar{\tilde{F}}(u^-_{i+1/2,j}, u^+_{i+1/2,j}) = \bar{\tilde{F}}(u_{i,j}, u_{i+1,j}) \tag{4.8}$$

$$= \frac{1}{2}[\tilde{F}(u_{i,j}) + \tilde{F}(u_{i+1,j})], \tag{4.9}$$

2. a standard local Lax-Friedrichs (LLF) scheme,

$$\bar{\tilde{F}}(u^-_{i+1/2,j}, u^+_{i+1/2,j}) = \frac{1}{2}[\tilde{F}(u^-_{i+1/2,j}) + \tilde{F}(u^+_{i+1/2,j}) - \max|\tilde{F}_u| \cdot (u^+_{i+1/2,j} - u^-_{i+1/2,j})], \tag{4.10}$$

$$u^-_{i+\frac{1}{2},j} = u_{i,j}, \quad u^+_{i+\frac{1}{2},j} = u_{i+1,j},$$

Universiteit Utrecht

- 3. a local Lax-Friedrichs scheme with reconstruction using a linear approximation (LLFR) [Zhengru Zhang and Tao Tang, 2002],

$$
\begin{aligned}
&u^-_{i+\frac{1}{2},j} = u_{i,j} + \frac{\Delta\xi}{2} s_{i,j}, \quad u^+_{i+\frac{1}{2},j} = u_{i+1,j} - \frac{\Delta\xi}{2} s_{i+1,j},\\
&s_{i,j} = \left(\operatorname{sign}(s^-_{i,j}) + \operatorname{sign}(s^+_{i,j})\right) \frac{\|s^-_{i,j} s^+_{i,j}\|}{\|s^-_{i,j}\| + \|s^+_{i,j}\|},\\
&s^-_{i,j} = \frac{u_{i,j} - u_{i-1,j}}{\Delta\xi}, \quad s^+_{i,j} = \frac{u_{i+1,j} - u_{i,j}}{\Delta\xi}.
\end{aligned}
\tag{4.11}
$$

Moving mesh PDE

The MMPDE6 [Weizhang Huang, 1994] in 2D reads

$$\text{MMPDE6:} \quad \begin{cases} \bar{\nabla} \cdot \bar{\nabla} \dot{x} = -\dfrac{1}{\tau_x} \bar{\nabla} \cdot (\mathbf{M} \bar{\nabla} x), \\ \bar{\nabla} \cdot \bar{\nabla} \dot{z} = -\dfrac{1}{\tau_z} \bar{\nabla} \cdot (\mathbf{M} \bar{\nabla} z). \end{cases} \tag{4.12}$$

Consider a time-dependent monitor function:

$$\mathbf{M} = \begin{bmatrix} M_1 & 0 \\ 0 & M_2 \end{bmatrix}, M_i = (1-\kappa)\gamma_i(t) + \kappa\, \omega_i, i = 1, 2, \tag{4.13}$$

$$\gamma_i(t) = \int_0^1 \int_0^1 \omega_i \mathrm{d}\xi \mathrm{d}\eta. \tag{4.14}$$

If the diagonal elements are identical, we get an adaptive mesh without directional control. When the monitor components ω_i are of the arc-length type or curvature type of u in each direction, a monitor with directional control can be obtained.

Smoothing strategy

A smoothing strategy based on a diffusive mechanism in [Weizhang Huang, 1997] is also employed,

$$[\mathcal{I} - \left(\sigma_\xi(\sigma_\xi + 1)(\Delta\xi)^2 \frac{\partial^2}{\partial\xi^2} + \sigma_\eta(\sigma_\eta + 1)(\Delta\eta)^2 \frac{\partial^2}{\partial\eta^2}\right)]\tilde{M} = M, \tag{4.15}$$

$$\vec{n} \cdot \nabla \tilde{M} = 0, \quad (\xi, \eta) \in \partial_\Omega, \tag{4.16}$$

We numerically show that the corresponding adaptive mesh admit quasi-uniformity properties:

$$\begin{cases} \text{Density ratio along } x\text{-direction:} & \dfrac{\sigma_\xi}{\sigma_\xi + 1} \leq \dfrac{\Delta x_{i+1}(t)}{\Delta x_i(t)} \leq \dfrac{\sigma_\xi + 1}{\sigma_\xi}, \\ \text{Density ratio along } z\text{-direction:} & \dfrac{\sigma_\eta}{\sigma_\eta + 1} \leq \dfrac{\Delta z_{j+1}(t)}{\Delta z_j(t)} \leq \dfrac{\sigma_\eta + 1}{\sigma_\eta}, \quad \forall t \in [0, T]. \end{cases} \tag{4.17}$$

Universiteit Utrecht

Adaptive meshes and density rations

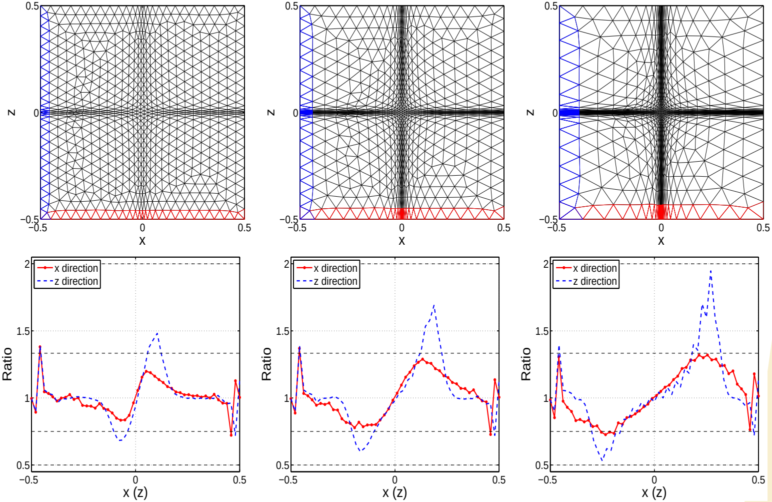

Figure 6: Adaptive meshes and density ratios for $\kappa = 0.25$ (left), $\kappa = 0.5$ (middle) and $\kappa = 0.75$ (right) with $\sigma_\xi = 3, \sigma_\eta = 1$.

Example 1

Solve the 1D MBLE in the z-direction with the central difference flux (4.8), the LLF flux (4.10) and the LLFR flux (4.11).

$$\begin{cases} G(u) = \dfrac{u^2}{u^2 + M(1-u)^2}(1 - C(1-u)^2), \\ D(u) = -\epsilon, \quad H(u) = \epsilon^2, \\ M = 0.5, C = 2, \epsilon = 10^{-3}, \tau = 2.5. \end{cases}$$

Example 1

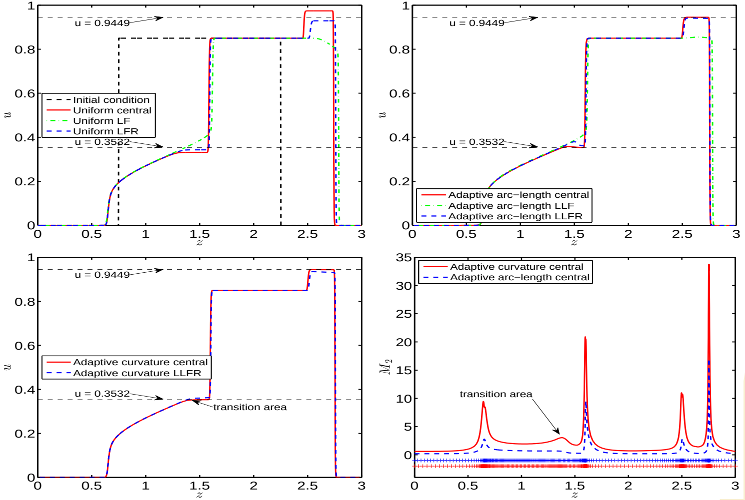

u = 0.9449
u = 0.3532
Initial condition
Uniform central
Uniform LF
Uniform LFR
Adaptive arc−length central
Adaptive arc−length LLF
Adaptive arc−length LLFR
Adaptive curvature central
Adaptive curvature LLFR
transition area
Adaptive curvature central
Adaptive arc−length central
transition area
u
z
M_2

Example 2

The 2D MBLE with dynamic capillary pressure term. The initial condition is of a cylindrical shape

$$u(x,z,0) = \begin{cases} 0.9, & x^2+y^2<0.5, \\ 0, & \text{otherwise}, \end{cases} \qquad (x,z)\in[-1.5,1.5]\times[-1.5,1.5]. \tag{4.18}$$

Results in 1D

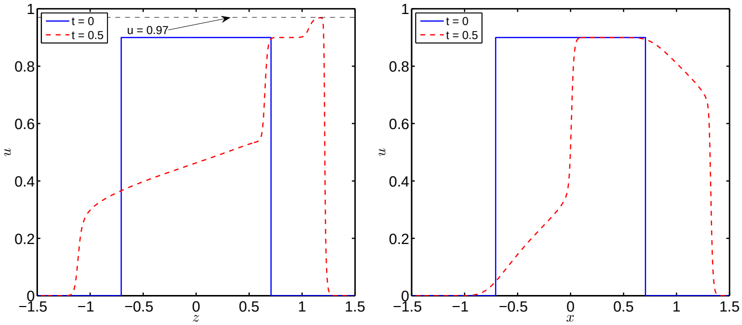

Figure 7: Resutls in 1D at $t = 0.5$.

Universiteit Utrecht

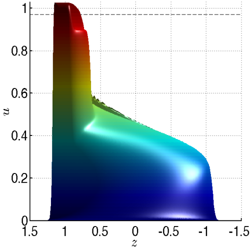

Uniform 301^2 central, 1.0253

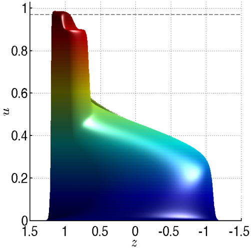

Uniform 1001^2 central, 0.9859

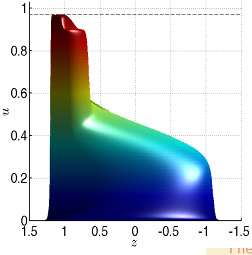

Adaptive 301^2 central, 0.9698

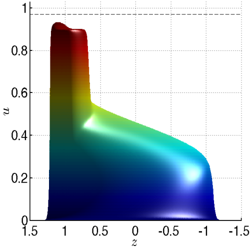

Uniform 301^2 LLFR, 0.9327

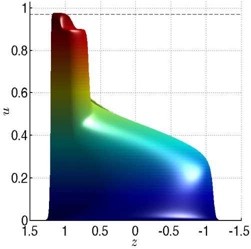

Uniform 1001^2 LLFR, 0.9768

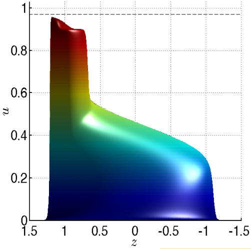

Adaptive 301^2 LLFR, 0.9571

2D simulation with a cubic initial condition

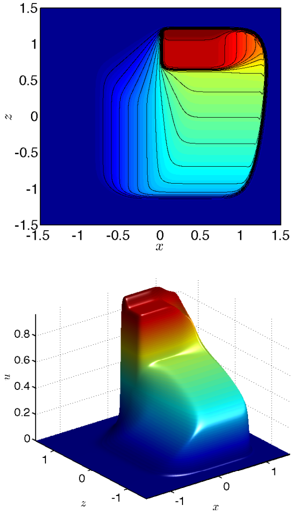

(a) Uniform 1001^2 LLFR plateau heigh ≈ 0.9670

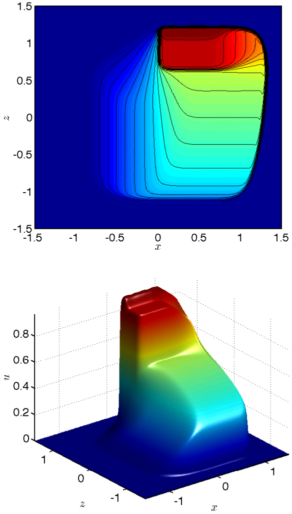

(b) Adaptive 301^2 Cental, plateau heigh ≈ 0.9695

Conclusions

- The moving mesh method successfully resolved the monotone and non-monotone solutions with high accuracy.
- To achieve the same accuracy, the moving mesh method needs approximately a factor of 5-10 fewer grid points than the uniform case.
- The arc-length monitor function has higher accuracy in steep regions, while the smoothed monitor function gives a better balance between the smooth and the steep regions.

Presented Results are part of:

Zhang H, Zegeling P A. A numerical study of two-phase flow models with dynamic capillary pressure and hysteresis[J]. Transport in Porous Media 116(2), 825-846 (2017)

Zhang H, Zegeling P A. Numerical investigations of two-phase flow with dynamic capillary pressure in porous media via a moving mesh method[J]. Journal of Computational Physics, 2017, 345: 510-527

Zhang H, Zegeling P A. A moving mesh finite difference method for non-monotone solutions of non-equilibrium equations in porous media[J]. Communications in Computational Physics, 2017, 22 (4), 935-964

Conclusions

- The moving mesh method successfully resolved the monotone and non-monotone solutions with high accuracy.
- To achieve the same accuracy, the moving mesh method needs approximately a factor of 5-10 fewer grid points than the uniform case.
- The arc-length monitor function has higher accuracy in steep regions, while the smoothed monitor function gives a better balance between the smooth and the steep regions.

Presented Results are part of:

Zhang H, Zegeling P A. A numerical study of two-phase flow models with dynamic capillary pressure and hysteresis[J]. Transport in Porous Media 116(2), 825-846 (2017)

Zhang H, Zegeling P A. Numerical investigations of two-phase flow with dynamic capillary pressure in porous media via a moving mesh method[J]. Journal of Computational Physics, 2017, 345: 510-527

Zhang H, Zegeling P A. A moving mesh finite difference method for non-monotone solutions of non-equilibrium equations in porous media[J]. Communications in Computational Physics, 2017, 22 (4), 935-964

Conclusions

- The moving mesh method successfully resolved the monotone and non-monotone solutions with high accuracy.
- To achieve the same accuracy, the moving mesh method needs approximately a factor of 5-10 fewer grid points than the uniform case.
- The arc-length monitor function has higher accuracy in steep regions, while the smoothed monitor function gives a better balance between the smooth and the steep regions.

Presented Results are part of:

Zhang H, Zegeling P A. A numerical study of two-phase flow models with dynamic capillary pressure and hysteresis[J]. Transport in Porous Media 116(2), 825-846 (2017)

Zhang H, Zegeling P A. Numerical investigations of two-phase flow with dynamic capillary pressure in porous media via a moving mesh method[J]. Journal of Computational Physics, 2017, 345: 510-527

Zhang H, Zegeling P A. A moving mesh finite difference method for non-monotone solutions of non-equilibrium equations in porous media[J]. Communications in Computational Physics, 2017, 22 (4), 935-964

References

David A DiCarlo. "Experimental measurements of saturation overshoot on infiltration". In: *Water Resources Research* 40.4 (2004), W04215.

CJ van Duijn, LA Peletier, and IS Pop. "A new class of entropy solutions of the Buckley-Leverett equation". In: *SIAM Journal on Mathematical Analysis* 39.2 (2007), pp. 507–536.

Mehdi Eliassi. "On continuum -scale numerical simulation gravity -driven fingers in unsaturated porous material". PhD thesis. 2001.

S Majid Hassanizadeh and William G Gray. "Mechanics and thermodynamics of multiphase flow in porous media including interphase boundaries". In: *Advances in water resources* 13.4 (1990), pp. 169–186.

Mahsanam Mirzaei and Diganta Bhusan Das. "Experimental investigation of hysteretic dynamic effect in capillary pressure–saturation relationship for two-phase

THANK YOU FOR YOUR ATTENTION!

Questions?

Universiteit Utrecht